

The Cost Scaling Analysis of Thermal Batteries Minimizing the Cost per kWh

Supplemental Information

Jordan D. Kocher¹, Jason Woods², Adewale Odukumaiya², Allison Mahvi^{2,3}, and Shannon K. Yee^{1,2*}

¹George W. Woodruff School of Mechanical Engineering, Georgia Institute of Technology, Atlanta, GA, USA

²National Renewable Energy Laboratory, Golden, CO, USA

³Department of Mechanical Engineering, University of Wisconsin, Madison, WI, USA

*Corresponding author. Email: shannon.yee@me.gatech.edu

Supplementary Note 1: Derivation of ΔSOC

The term ΔSOC is the fraction of total thermal battery capacity than can be extracted during discharge. For any thermal battery, ΔSOC can be found by starting with unity, then subtracting the fraction of heat lost during storage, and then subtracting the fraction of thermal capacity that remains within the battery when it reaches the cutoff temperature. The total volumetric energy density of the PCM material (S_{PCM}) is the volumetric enthalpy change between the temperature the PCM is charged to, T_{chg} , and the cutoff temperature, T_{cutoff} .

To understand the thermal losses in more detail, we begin by analyzing the heat that leaks into the thermal battery during storage (this assumes cold storage; for hot storage, heat would leak out of the battery during the storage period). We first assume that the thermal mass of the heat exchangers and HTF within the battery are negligible compared to the PCM (*i.e.*, there is significantly more PCM thermal mass than heat exchanger and HTF thermal mass). Next, we assume that the PCM can be approximated with the lumped capacitance model. This is valid when

the PCM internal resistance is small relative to the insulation resistance, which will likely be the case for two reasons: (i) thermal storage media must be thermally conductive to extract most of the capacity during discharging, and (ii) the external thermal resistance must be high to prevent significant losses during storage. Finally, we assume that the storage losses are entirely sensible (*i.e.*, the PCM does not undergo any phase change while it is being stored). For latent heat storage, this would mean the PCM is charged by cooling it far enough below the melting temperature that it wouldn't melt when heat leaks in during storage (or, for hot storage, the PCM is heated sufficiently above the freezing temperature that it does not freeze during storage). By making these assumptions, the rate of heat transfer (loss) to the PCM during storage is

$$\dot{Q}_S = \frac{A_{ins}}{R_{ins}}(T_{surr} - T_{PCM})$$

. The rate of heat transfer during storage gives the rate of change of the

PCM temperature, $\dot{Q}_S = V_{PCM}\rho_{PCM}c_{p,PCM,s} \frac{dT_{PCM}}{dt}$, where $c_{p,PCM,s}$ is the specific heat of the solid

phase PCM. This can be rewritten as $\frac{dT_{PCM}}{T_{surr} - T_{PCM}} = \frac{A_{ins}}{V_{PCM}R_{ins}\rho_{PCM}c_{p,PCM,s}} dt$, where the characteristic length $V_{PCM}/A_{ins} = L_S$ appears. Integrating reveals that the temperature at the end

of storage (which is also the beginning of the discharging process) is

$$T_d = T_{surr} - (T_{surr} - T_{chg}) \exp\left(-\frac{1}{L_S R_{ins} \rho_{PCM} c_{p,PCM,s}} t_s\right)$$

. This means that the storage losses can be

written in terms of L_S as:

$$f_1 = \frac{\rho_{PCM} c_{p,PCM,s}}{S_{PCM}} \left(T_{surr} - T_{chg} + (T_{surr} - T_{chg}) \exp\left(-\frac{1}{L_S R_{ins} \rho_{PCM} c_{p,PCM,s}} t_s\right) \right),$$

where t_s is the

storage time, or the time in between the end of charging and beginning of discharging. For all of

the analyses in this work, the charging temperature was $T_{chg} = -10$ °C. This value was chosen as it was sufficiently low that the PCM would never begin melting during the storage process for any of the scenarios we analyzed.

Next, the discharging process thermal losses are considered. During discharge, heat is transferred to the PCM through the heat exchanger, and as the heat conducts through the PCM, the HTF temperature increases until it reaches the cutoff value. Natural convection is neglected in the PCM, an approximation that was also made by Woods *et al.* in their thermal Ragone work (which notably considers the same geometry as this work) and was justified by their experimental validation of their model¹. When the cutoff temperature is reached, the heat has conducted through some of the PCM volume, $V_{PCM,p}$. Dividing this volume by the heat exchanger surface area yields another characteristic length, which is the cutoff thermal penetration depth, $L_p = V_{PCM,p}/A_{HX}$, for which we derive an expression in Supplementary Note 2. If the PCM is thicker than the cutoff penetration depth ($L_C > L_p$), then the PCM is essentially semi-infinite, and none of the PCM beyond L_p has contributed any thermal capacity. As such, a thermal battery would never be designed such that $L_C > L_p$, because of the higher system cost, though we do provide results for $L_C > L_p$ in the main text to illustrate its higher system cost. In latent heat thermal storage, the thermal penetration length is simply the location of the melting front.

The functional form of the unextractable capacity depends on the type of thermal storage (sensible, latent, or thermochemical). In this work, we focus on latent heat thermal storage (though we provide an analysis of sensible heat thermal storage in Supplementary Note 12). Woods *et al.*¹ created an exact numerical simulation of the melting of a rectangular PCM layer with constant heat flux, which can be used to precisely calculate ΔSOC . However, a simplified analytical

approximation can provide deeper insight that complements the numerical simulation without sacrificing much accuracy. To obtain a simple analytical approximation for the unextractable capacity, we assume the PCM has negligible sensible capacity relative to the latent capacity (a small Stefan number). Then, the unextractable capacity is simply the product of the latent heat and the volume of PCM that does not melt before the cutoff is reached. Since the thermal penetration depth in our analysis is the melting front, all PCM before the cutoff penetration depth melts and all PCM beyond the penetration depth remains frozen. This means the unextractable capacity is

$f_2 = \left(1 - \frac{L_p}{L_C}\right) \frac{h_{SL}}{S_{PCM}/\rho_{PCM}}$, where h_{SL} is the latent heat of melting. In this simplified analytical approximation, if the melting front reaches L_C before the cutoff temperature is reached, then all of the latent capacity has been extracted. Any sensible capacity extracted after the melting front reaches the edge of the PCM is negligible. Neglecting this sensible capacity allows for a simple, analytical expression for ΔSOC that cannot otherwise be obtained with a loss of accuracy of less than 10% (see the Supplementary Note 5). Subtracting the storage losses and unextractable capacity from unity yield an expression for ΔSOC .

$$\Delta SOC = 1 - \frac{\rho_{PCM} c_{p,PCM,s}}{S_{PCM}} \left((T_{surr} - T_{chg}) \left(1 + \exp \left(- \frac{1}{L_S R_S'' \rho_{PCM} c_{p,PCM,s}} t_s \right) \right) \right) + \left(1 - \frac{L_p}{L_C} \right) h_{SL} \quad (S1)$$

Supplementary Note 2: Derivation of thermal penetration depth (melting front location) in a semi-infinite PCM slab

To find the unextractable latent capacity of a thermal battery, 1-D melting of a semi-infinite slab of PCM is considered. At the beginning of the discharging process, it is assumed that the

entire PCM is at a uniform temperature of T_m . When discharging begins, a constant heat flux of q'' is imposed as the boundary of the PCM slab. When a small Stefan number is assumed, the liquid phase absorbs no heat; all of the heat introduced at the boundary conducts through the liquid phase and is absorbed into the moving melting front. This makes the melting process quasi-steady, giving

$$\frac{\partial^2 T_L}{\partial x^2} = 0$$

a governing equation of $\frac{\partial^2 T_L}{\partial x^2} = 0$, where T_L is the liquid phase temperature. Integration gives $T_L = C_1 x + C_2$. The location of the melting front is $x_i(t)$, at which the liquid phase temperature is

$T_L(x_i) = T_m$. This gives $C_2 = T_m - C_1 x_i$. The constant heat flux boundary condition is

$q'' = -k_L \frac{\partial T_L}{\partial x} = -k_L C_1$. Evaluating gives $T_L = \frac{q''}{k_L}(x_i - x) + T_m$, though $x_i(t)$ is not yet known. The

interface energy condition is $-k_L \frac{\partial T_L}{\partial x} = \rho_L h_{SL} \frac{dx_i}{dt}$. This gives $x_i = \frac{q''}{\rho_L h_{SL}} t$.

The heat exchanger has some finite heat transfer coefficient; as such, there is a nonzero temperature drop across it. The temperature of the HTF on the one side of the heat exchanger is related to the temperature of the PCM on the other side: $q'' = U_{HX}(T_{HTF} - T_{L,0})$. Evaluating

T_{cutoff} for T_{HTF} gives the following expression: $q'' = U_{HX} \left(T_{cutoff} - \frac{q''}{k_L} x_{i,cutoff} - T_m \right)$. $x_{i,cutoff}$ is

equivalent to L_{melt} , which is the melting front location when the cutoff temperature is reached in

a semi-infinite slab of PCM. Rearranging gives $L_{melt} = k_L \left(\frac{T_{cutoff} - T_m}{q''} - \frac{1}{U_{HX}} \right)$. L_{melt} is the

maximum thermal penetration depth for a given PCM thermal conductivity, melting temperature, heat flux, cutoff temperature, and heat exchanger heat transfer coefficient.

In a finite slab of PCM, the thermal penetration depth either reaches the end of the slab ($L_p = L_c$), or it is the melting front location derived above ($L_p = L_{melt}$). This is summarized in Eq. (S2).

$$L_p = \begin{cases} L_c, & L_c < L_{melt} \\ L_{melt}, & L_c \geq L_{melt} \end{cases} \quad (\text{S2})$$

Using the expression for L_{melt} , Eq. (S2) can also be written in dimensionless form as:

$$\frac{L_p}{L_c} = \min \left\{ 1, \frac{k_L}{U_{HX} L_c} \left(\frac{U_{HX} (T_{cutoff} - T_m)}{q''} - 1 \right) \right\} \quad (\text{S3})$$

Eq. (S3) is used to find L_p for constant q'' . However, it is more useful to find L_p for a fixed C-rate, in which case q'' varies with L_c (since $q'' = S_{PCM} C_{rate} L_c$). Then, Eq. (S3) can be rewritten as Eq. (S4), and L_p becomes a function of L_c .

$$\frac{L_p}{L_c} = \min \left\{ 1, \frac{k_L}{U_{HX} L_c} \left(\frac{U_{HX} (T_{cutoff} - T_m)}{S_{PCM} C_{rate} L_c} - 1 \right) \right\} \quad (\text{S4})$$

Eq. (S4) was derived for melting, which corresponds to cold storage (the PCM is stored at a low temperature and then melts while absorbing heat during discharge). For hot storage (*i.e.*, solidification), the general heat transfer problem remains the same, except T_L becomes T_S (the temperature profile within the solidifying domain), the constant heat flux boundary condition

becomes $q'' = -k_S \frac{\partial T_S}{\partial x} = -k_S C_1$, and the interface energy boundary condition becomes

$-k_S \frac{\partial T_S}{\partial x} = \rho_S h_{SL} \frac{dx_i}{dt}$. Solving the governing equation with these new boundary conditions yields

the same equation as Eq. (S4), but with solid phase properties for the thermal conductivity and density.

The optimal PCM thickness is often equal to the maximum thermal penetration depth ($L_C = L_{melt}$), in which case we refer to the PCM thickness as $L_{C,p}$. However, L_{melt} is itself dependent on L_C when the C-rate is fixed, producing a quadratic equation with a root of $L_{C,p}$:

$$L_{C,p} = \frac{k_{PCM}}{2U_{HX}} \left(\sqrt{4 \frac{U_{HX}^2 (T_{cutoff} - T_m)}{k_{PCM} S_{PCM} C_{rate}} + 1} - 1 \right) \quad (S5)$$

where k_{PCM} is the thermal conductivity of the liquid phase for cold storage and the thermal conductivity of the solid phase for hot storage. $L_{C,p}$ is the value of L_C that would result in heat penetrating to the PCM furthest from the heat exchanger at the instant the cutoff temperature is reached.

Supplementary Note 3: Shortcomings of the simple model

From Eq. (3) of the main text, the PCM and insulation costs scale with $\frac{1}{\Delta SOC}$, while the heat exchanger costs scale with $\frac{1}{L_C \Delta SOC}$. In our simple analytical model, ΔSOC is constant for $0 < L_C \leq L_p$, meaning that the PCM and insulation costs are constant for $0 < L_C \leq L_p$, while the heat exchanger costs are minimized at $L_C = L_p$. Thus, the optimal value of L_C is always L_p . However, Woods *et al.* showed that in a real PCM, ΔSOC decreases slightly with increasing L_C (due to the sensible heat capacity of the liquid).¹ Therefore, in a real thermal battery, the PCM and insulation costs are minimized when the PCM layer is very thin, while the heat exchanger cost is still minimized at $L_C = L_p$. If the PCM or insulation cost scaling factors are comparable to the heat

exchanger cost scaling factor, then the optimal L_C that minimizes the device cost will lie somewhere between 0 and L_p . The more expensive the heat exchanger, the closer it will be to L_p . When the heat exchanger in the thermal battery is expensive (which is often the case), our simple analytical approximation does not significantly overpredict the optimal value of L_C . In Supplementary Note 5, we quantify this error between the costs that result from our simple analytical expression and from the numerical solution.

Supplementary Note 4: Limit on characteristic length of thermal storage

The cost scaling analysis reveals that the device cost monotonically decreases with L_S ; therefore, an infinitely large L_S is desirable. This is illustrated in Figure S1, where two different thermal batteries with the same storage capacity are pictured. Both have the same amount of PCM (V_{PCM}) and the same total heat exchanger area (A_{HX}), meaning that L_C is the same for both. However, the difference between the two is the external surface area that needs to be insulated. In Figure S1a, the area that must be insulated is large, because only two PCM layers are used and the battery width (W) is large. However, in Figure S1b, the same amount of heat exchanger surface area is instead divided into thirds. Likewise, the amount of PCM is the same in both Figure S1a and Figure S1b, but in Figure S1b it is divided into six layers (the interior PCM sections count as two layers each). This results in a thermal battery that is closer in shape to a cube, giving a smaller external surface area per unit volume PCM (*i.e.*, larger L_S).

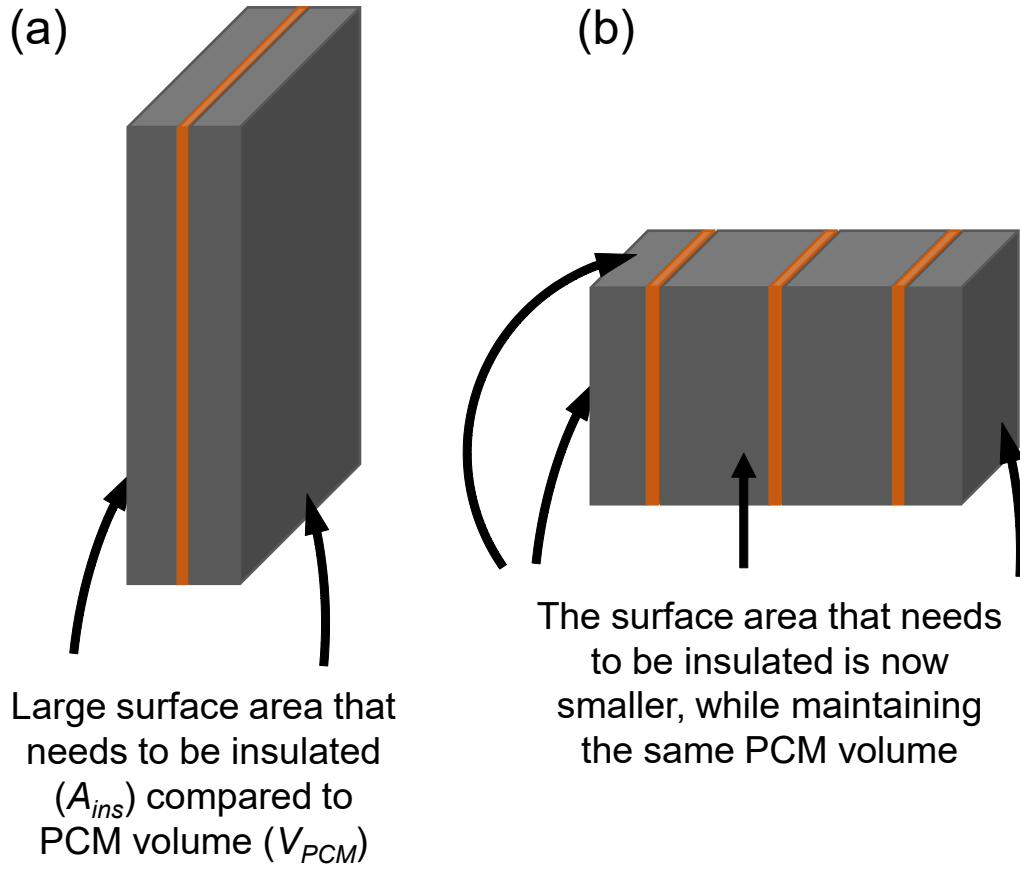


Figure S1. Two different thermal batteries with the same capacity, PCM volume, heat exchanger area, and L_S are illustrated. However, in (a) the battery geometry results in a larger external surface area, requiring more insulation, and more area through which heat can escape. Meanwhile, in (b) the battery geometry results in less surface area that needs to be insulated.

However, when implementing the device in practice, the total storage capacity (which is proportional to V_{PCM}) must be designed to fit the needs of the thermal load. Thus, W and N are selected to give the device the maximum L_S for the desired storage capacity. This can be found by

$$N = \frac{Cap}{S_{PCM} W^2 L_C}$$

first substituting

$$W_{opt} = \sqrt{\frac{Cap}{S_{PCM}} \left(1 + \frac{t_{HX}}{L_C}\right)} \quad (S6)$$

where t_{HX} is the thickness (x-direction length as depicted in Fig. 3 of the main text) of the heat exchanger and Cap is the desired thermal storage capacity of the thermal battery. For the fixed battery capacity, this also corresponds to the number of layers that maximizes L_S :

$$N_{opt} = \frac{Cap^{1/3}}{S_{PCM}^{1/3} L_C \left(1 + \frac{t_{HX}}{L_C}\right)^{2/3}} \quad (S7)$$

The expression for the maximum L_S for the geometry illustrated in Fig. 1 of the main text is:

$$L_{S,max} = \frac{Cap^{1/3}}{6S_{PCM}^{1/3} \left(1 + \frac{t_{HX}}{L_C}\right)^{2/3}} \quad (S8)$$

The optimal battery width and number of PCM layers are used to find the maximum possible L_S for a fixed capacity. Notably, the number of PCM layers must be an integer value, which will cause the true maximum allowable L_S to deviate slightly from $L_{S,max}$ due to rounding.

Supplementary Note 5: Quantifying error between analytical approximation and numerical solution

To quantify the validity of our analytical approximation for the loss in thermal capacity at cutoff (f_2), we compared our results to results that we obtained from the numerical model developed by Woods *et al.*¹ (Figure S2). We are only comparing the loss of unobtainable thermal capacity due to the presence of thermal resistances (f_2), not the loss of thermal capacity due to heat transfer with the ambient during storage (f_1) since Woods *et al.* did not consider the latter.

To make this comparison, we ran the numerical simulation code provided by Woods et al., using the default values programmed into the code (*i.e.*, cutoff temperature of 12 °C, tetradecane/graphite PCM, propylene glycol/water HTF, C-rate of 1 h⁻¹), with the exception of several values. First, we changed the PCM thermal conductivity to 10 W m⁻¹ K⁻¹, to match our analytical analysis. For our analyses in the main text we used an initial PCM temperature of -10 °C at the beginning of storage and then calculated the temperature at the beginning of discharge based on thermal losses during storage. For this analysis, since we were not considering the storage period, we assumed the PCM temperature at the beginning of discharge was 4 °C (for both the analytical and numerical analysis). The numerical analysis code requires an input for the temperature drop of the HTF across the thermal battery; we set this value to 1 °C to best match our analytical analysis, since our analytical model approximates the HTF temperature as being constant across the thermal battery. Finally, we varied the PCM thickness between 3.3×10^{-4} m and 9.5×10^{-2} m (though the numerical model was only able to analyze a subset of this range, because it was running out of memory when analyzed for some of the PCM thicknesses). In addition, to make a direct comparison between the analytical and numerical models, we altered the numerical model so that instead of calculating the convective heat transfer coefficient from a pre-programmed correlation, it used a constant heat transfer coefficient of 571.6 W m⁻² K⁻¹ across the entire length of the heat exchanger (as our analytical analysis uses a constant heat transfer coefficient of the same value). ΔSOC was obtained using both the analytical and numerical analyses and is plotted in Figure S2.

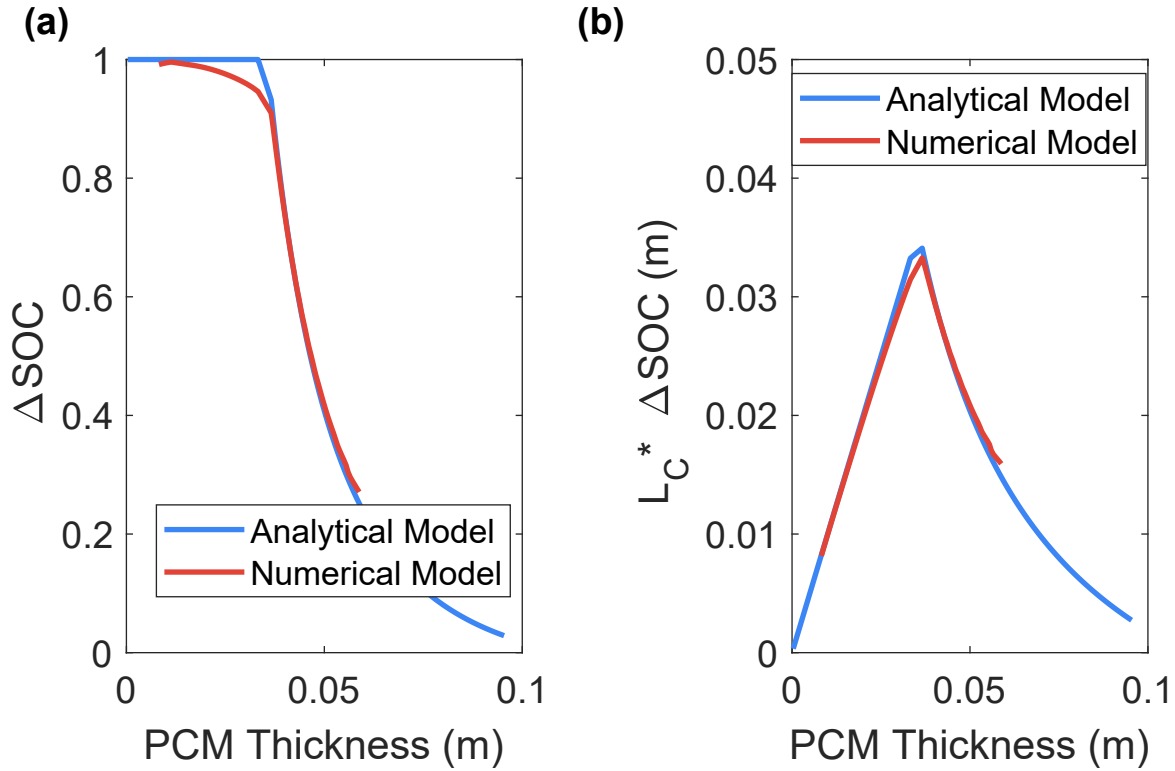


Figure S2. Difference between the numerical solution (developed by Wood *et al.*²) and analytical approximation (developed in this work) of the unobtainable SOC left within the PCM of a thermal storage device when cutoff is reached. In (a), the quantity plotted is ΔSOC , which is a relevant quantity for the PCM's contribution to system cost; in (b), the quantity plotted is the product of PCM thickness (L_C) and ΔSOC , which is a quantity relevant to the heat exchangers' contribution to system cost. The L_C^* plotted in this figure assumes no losses during storage ($\eta = 1$).

In Figure S2, we plot both ΔSOC (a) and $L_C \times \Delta SOC$ (b) as a function of L_C . When distributing the $1/\Delta SOC$ term in Eq. (3) of the main text, the PCM cost scaling factor is proportional to ΔSOC^{-1} , while the heat exchanger cost scaling factor is proportional to $(L_C \times \Delta SOC)^{-1}$. Thus, when the heat exchanger cost is great (as was the case for the systems we analyzed in the main text), the $L_C \times \Delta SOC$ term is more important, while the term ΔSOC is more important when PCM costs are high. Figure S2 shows that the analytical and numerical models are in very good agreement; the analytical model differs from the numerical model by no more than 6%. In fact,

Figure S2b shows that the maximum thermal penetration depth ($L_{c,p}$) is the same between the analytical and numerical models. The reason for the small discrepancy between the two models is that the analytical model neglects the sensible heat capacity of the liquid PCM (which was necessary to obtain a simple analytical expression), while the numerical model includes the liquid phase sensible capacity.

To illustrate that our analytical model is suitable for our cost scaling analysis, we recreated Fig. 2 from the main text in Figure S3, but in Figure S3 we used the results for ΔSOC that were obtained from the numerical model as well as the analytical model. In Figure S3, we plot the dimensionless system cost, G/G_0 , as a function of PCM thickness, as was done in Fig. 2 of the main text. However, in Fig. 2 we plotted curves of various PCM thermal conductivity and latent heat; in Figure S3 we look at a single PCM thermal conductivity ($10 \text{ W m}^{-1} \text{ K}^{-1}$) and latent heat (167 kJ kg^{-1}). From Figure S3, the minimum dimensionless cost differs by only 4%, and the system cost is minimized at the same PCM thickness, indicating that the results from the analytical model used in the main text are accurate.

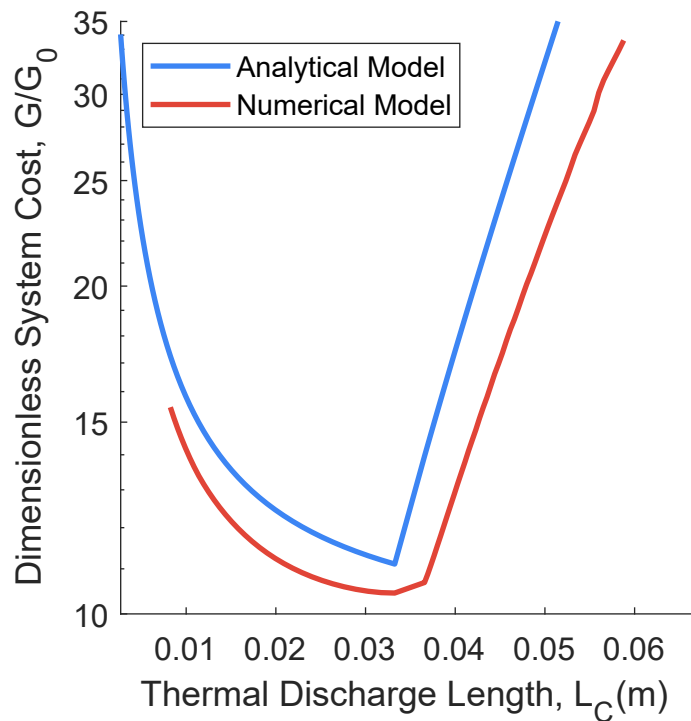


Figure S3. Comparison of dimensionless system cost as determined from the analytical and models for .

Scenarios where the analytical model would not be suitable include when the sensible heat of the PCM liquid phase is very high, the heat exchanger cost is low, or the mass flow rate of the HTF is low enough that the HTF temperature varies greatly across the thermal battery. In these cases, the more accurate numerical model should be used. In Supplementary Note 9 we provide a similar plot as Figure S3, but we instead consider the scenario where the heat exchanger is cheap; as such, we are required to use the numerical model for that particular analysis.

Supplementary Note 6: Insulation cost and thermal resistance

When generating the plots in this paper, R-30 fiberglass was considered for the insulation, which corresponds to $R''_{ins} = 5283 \text{ m}^2 \text{ K kW}^{-1}$. From Home Depot³, this insulation has an areal cost of $\$122.11 \text{ m}^{-2}$; dividing by R''_{ins} gives $c_{ins} = \$2.3 \times 10^{-2} \text{ kW m}^{-4} \text{ K}^{-1}$.

Supplementary Note 7: Sensitivity analysis of graphite cost

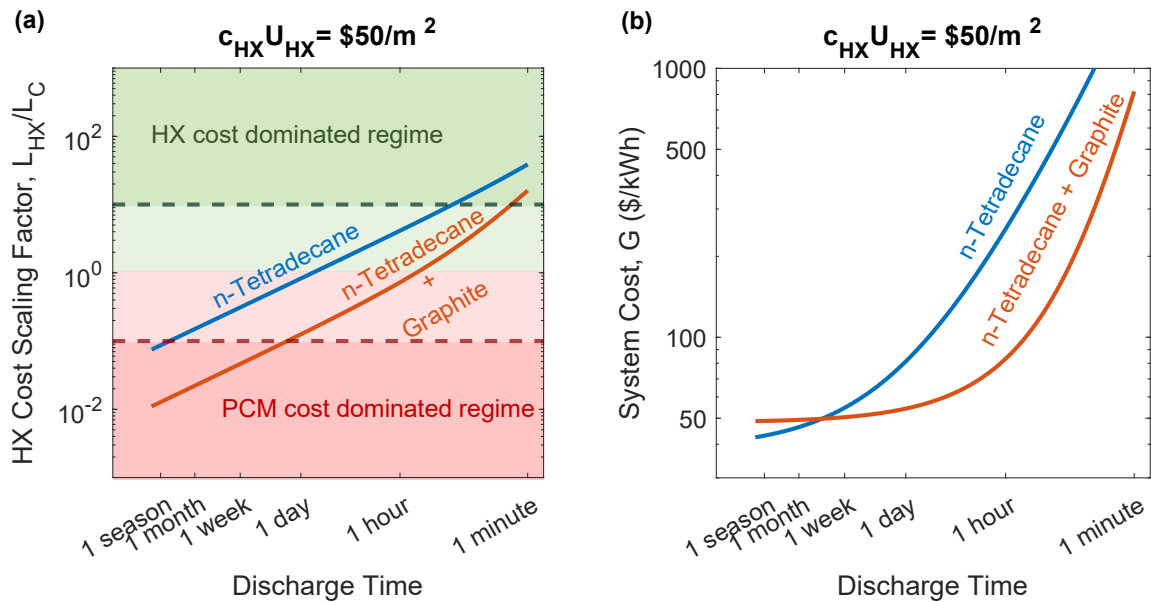


Figure S4. Heat exchanger cost scaling factor (a) and system cost (b) as a function of C-rate, with a graphite cost of $\$1/\text{kg}$.

In Fig. 6 of the main text, we present the heat exchanger cost scaling factor and system cost as a function of C-rate. In Fig. 6 of the main text, we assume a graphite cost of $\$2/\text{kg}$. However, other papers have used a graphite cost of about $\$1/\text{kg}$. As such, we provide Figure S4 which uses a graphite cost of $\$1/\text{kg}$. Upon comparison to Fig. 6 of the main text, it is clear that the results for n-Tetradecane are relatively insensitive to graphite cost.

Supplementary Note 8: Sensitivity analysis of heat exchanger cost

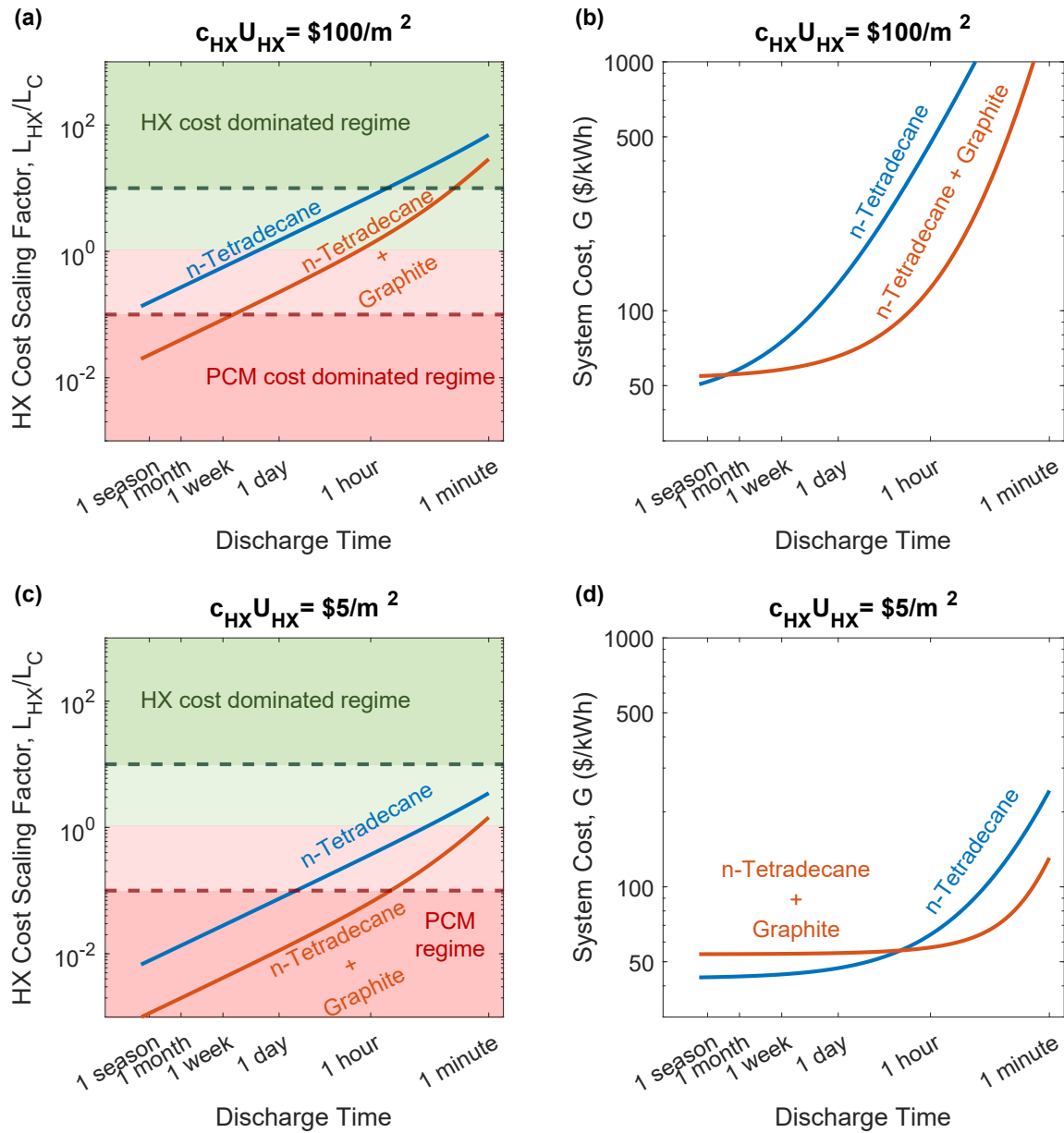


Figure S5. Heat exchanger cost scaling factor for a heat exchanger cost of $\$100/m^2$ (a) and $\$5/m^2$ (c). Thermal battery system cost for a heat exchanger cost of $\$100/m^2$ (b) and $\$5/m^2$ (d).

In Fig. 6 of the main text, we found the heat exchanger cost scaling factor and thermal battery cost for a heat exchanger cost of $\$50/m^2$ and $\$10/m^2$. However, the areal cost of heat exchangers often varies widely from one system (and one vendor) to another. As such, we provide results for $\$100/m^2$ in Figure S5(a-b). In addition, it is interesting to explore the scenario where

heat exchanger costs fall dramatically to \$5/m², perhaps due to improvements in manufacturing of low-cost heat exchanger materials (like plastics); these results are given in Figure S5(c-d).

Supplementary Note 9: Effect of L_C on thermal battery cost when PCM cost is significant

In Fig. 2 of the main text of this work, we plotted the dimensionless cost of a thermal battery as a function of the PCM thickness. In Supplementary Note 5 we performed the same analysis but compared the results from our analytical model for ΔSOC to the numerical model developed by Woods *et al.*¹ However, in both of those cases, the heat exchanger was very expensive, so the optimal PCM thickness was the same for the analytical and numerical model results, and it coincided with the maximum thermal penetration depth ($L_{C,p}$), which is also the melting front location at the instant the cutoff temperature is reached. However, when the PCM is costly relative to the heat exchanger, the optimal PCM thickness will be thinner than $L_{C,p}$. This is illustrated in Figure S6, which was generated using the same values as Figure S3, except the heat exchanger cost c_{HX} was reduced by an order of magnitude. In Figure S6, the analytical model predicts that the minimum system cost will occur at exactly $L_C = L_{C,p}$. However, the more accurate numerical model (which accounts for the sensible heat of the liquid phase) indicates that the minimum cost occurs at a smaller PCM thickness than $L_{C,p}$, which is due to the value of accessing that extra capacity from the liquid phase sensible heat when the PCM is expensive. However, it should be noted that even though the optimal PCM thickness differs significantly between the analytical and numerical results, the actual cost does not change much between the two thicknesses. As such, the cost penalty is not large when using the analytical model and oversizing the PCM (though this

penalty increases as the PCM becomes more and more expensive or as the heat exchanger becomes less expensive).

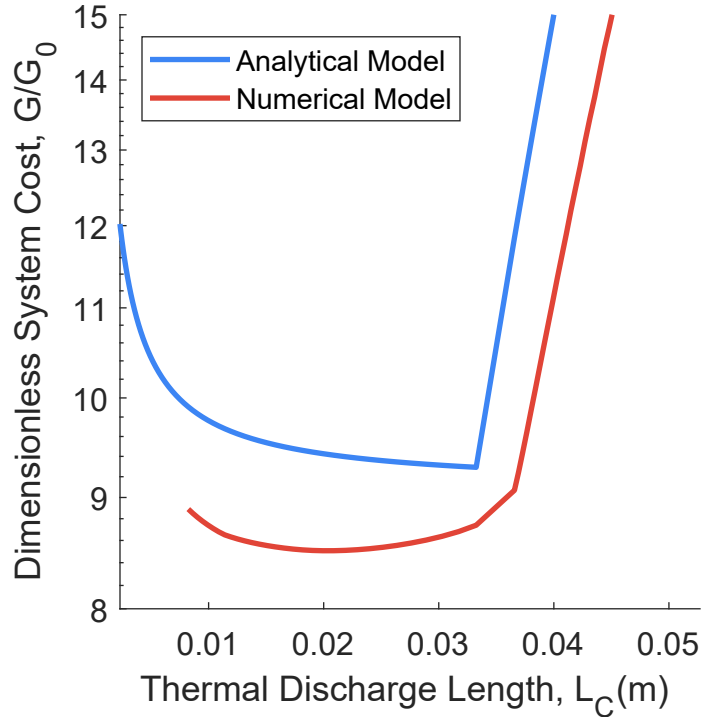


Figure S6. The dimensionless system cost, plotted as function of PCM thickness, using the analytical and numerical models for $\tau = 6 \times 10^{-3}$ m. At this value, the heat exchanger is cheap relative to the PCM, so the optimal PCM thickness is less than the maximum thermal penetration depth, as indicated by the numerical model results. However, because the analytical model does not include the sensible heat of the PCM liquid phase, it still predicts that the optimal thickness is the maximum thermal penetration depth.

Supplementary Note 10: Moving between two cost regimes

In Fig. 5 of the main text, we present a cost regime map with PCM figures-of-merit that correspond to regimes where one particular cost dominates the total system cost. Some PCM material properties are present in multiple regimes, but the power with which they scale varies. For example, the latent heat of the PCM appears in the FOM in all three regimes, but in the PCM

(volumetric) cost dominated regime, the FOM scales with h_{SL}^1 , while in the heat exchanger cost dominated regime the FOM scales with $h_{SL}^{1/2}$, and in the insulation cost dominated regime the FOM scales with $h_{SL}^{2/3}$.

To illustrate the effect this has on thermal battery cost, we provide an analysis of an example scenario in this section. For this example, we want to illustrate how the thermal battery cost, G , changes as h_{SL} varies in two different regimes. We have chosen to provide results for a cost that moves between the PCM and heat exchanger cost dominated regimes; as such, we set the insulation cost to $c_{ins} = \$0 \text{ kW m}^{-4} \text{ K}^{-1}$ to eliminate the effect that insulation has on the total system cost. Next, we chose cost and material properties that would allow us to illustrate the scenario where changing the latent heat value would cause the system cost to move between different cost regimes. Then, we plotted the thermal battery cost vs h_{SL}^{-1} for the PCM cost dominated regime, based on the FOM for that regime (Figure S7b), and we also plotted the thermal battery cost vs $h_{SL}^{-1/2}$ for the heat exchanger cost dominated regime, based on the FOM for that regime (Figure S7a). As seen in Figure S7, the thermal battery cost does indeed scale with $h_{SL}^{-1/2}$ when in the heat exchanger cost dominated regime, while it instead scales with h_{SL}^{-1} when in the PCM cost dominated regime.

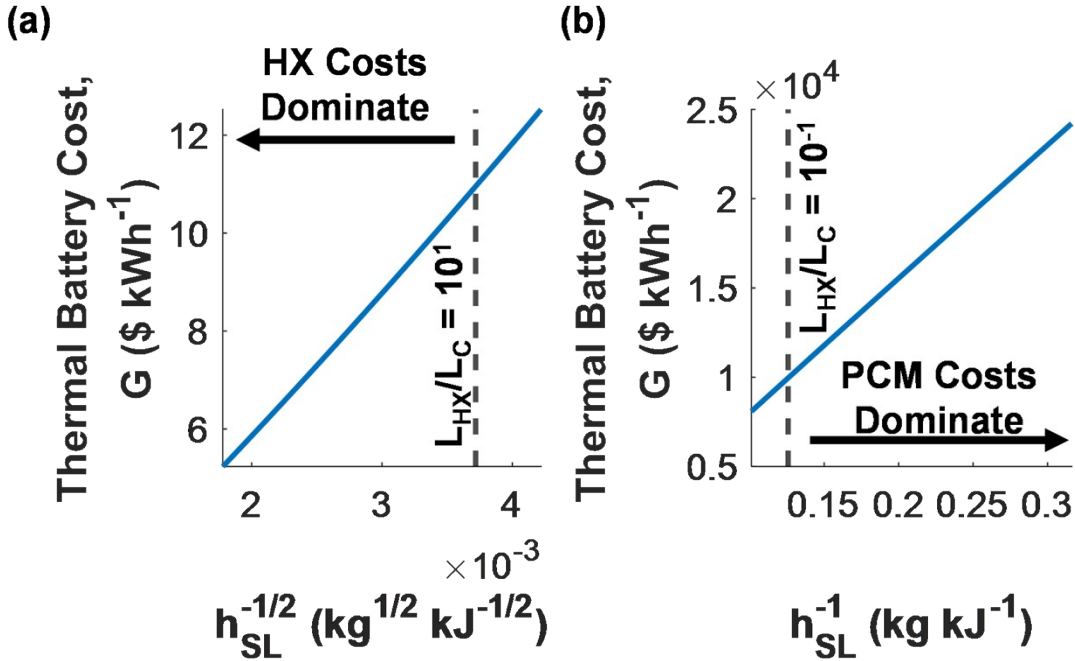


Figure S7. Thermal battery cost in the heat exchanger cost dominated regime (a) and the PCM cost dominated regime (b). In the heat exchanger cost dominated regime, the system cost scales with $h_{SL}^{-1/2}$, while in the PCM cost dominated regime, the system cost scales with h_{SL}^{-1} . The values used for this thermal battery are $c_{PCM} = \$20 \text{ kg}^{-1}$, $\Delta T = 4.6 \text{ }^\circ\text{C}$, $k_{PCM} = 1 \text{ W m}^{-1} \text{ K}^{-1}$, $L_C = \$6.43 \text{ K kW}^{-1}$, $k_{HX} = 16.48 \text{ kW m}^{-2} \text{ K}^{-1}$, $L_C = \$0 \text{ kW m}^{-4} \text{ K}^{-1}$; the remaining values are the same as the ones used in Fig. 5 of the main text.

We also wanted to illustrate that in one regime a particular property might appear in the FOM, while in another regime it does not appear at all. To illustrate this, we analyzed the effect that the thermal conductivity of the PCM has on system cost, as the FOM scales with $k_{PCM}^{1/2}$ when heat exchanger costs dominate but does not scale with k_{PCM} at all when PCM costs dominate. To illustrate this effect, we provide Figure S8, which plots filled contours of thermal battery cost as a function of PCM latent heat and PCM thermal conductivity. We also provide contours of L_{HX}/L_C (solid black lines) to indicate the different cost regime regions. When the PCM cost dominates ($L_{HX}/L_C < 0.1$), the thermal battery cost is barely affected by the PCM thermal conductivity, but it is a strong function of the latent heat. Meanwhile, when heat exchanger costs dominate (

$L_{HX}/L_C > 10$), both thermal battery cost changes both as a function of thermal conductivity and latent heat.

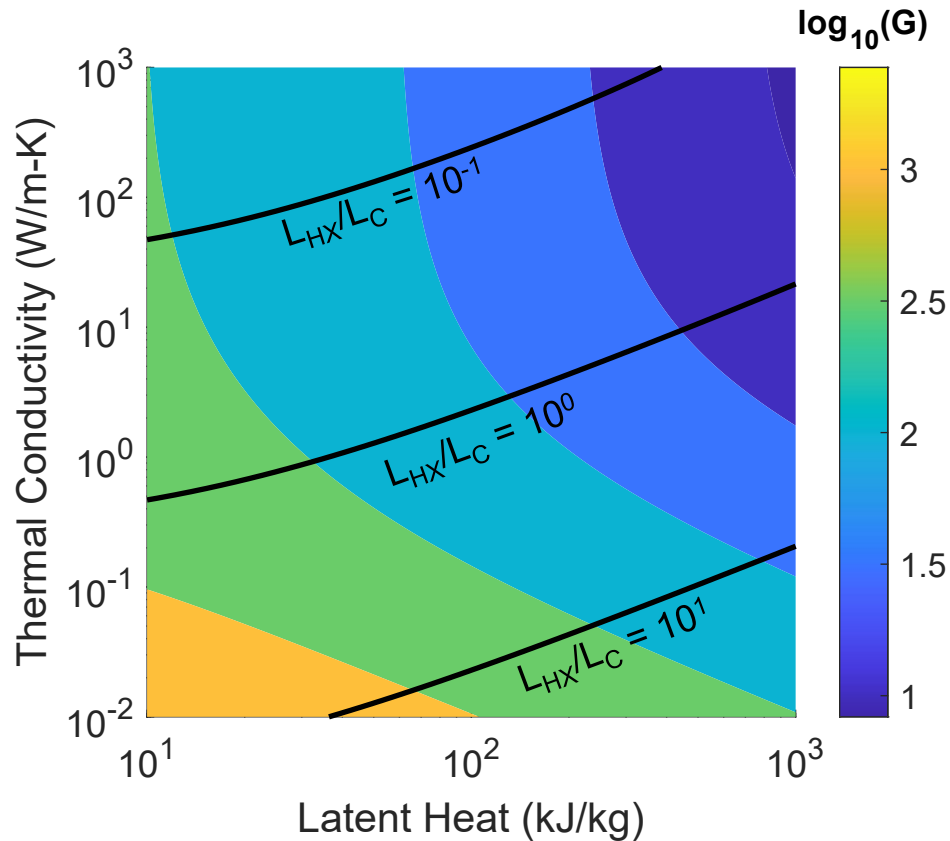


Figure S8. Contour plot of the logarithm of thermal battery cost () as a function of PCM latent heat and PCM thermal conductivity. Solid black lines are contours of the heat exchanger cost scaling factor. When PCM costs dominate (small heat exchanger cost scaling factor), the thermal conductivity has little effect on the thermal battery cost, while the latent heat has a great effect. Meanwhile, when heat exchanger costs dominate, both thermal conductivity and latent heat effect the thermal battery cost. The values used to construct this plot are the same as the ones used in Figure S7, except for thermal conductivity, which was varied in this plot.

Supplementary Note 11: PCM thermal battery with cylindrical geometry

While the thermal battery geometry considered in the main text of this work consists of rectangular PCM layers, other thermal battery geometries exist as well. To illustrate that the

general framework of our cost scaling analysis can be applied to other thermal battery geometries, we provide an analysis of a simple cylindrical geometry PCM thermal battery in this section. Eq. (3) of the main text applies to any thermal battery (sensible heat, latent heat, or thermochemical) of any geometry (rectangular, cylindrical, etc...). The only aspects of the cost scaling analysis that change between different thermal batteries are the functional forms of the characteristic lengths L_C and L_S , as well as the way ΔSOC changes as a function of these characteristic lengths. The simple cylindrical PCM thermal battery that we analyze in this section is depicted in Figure S9.

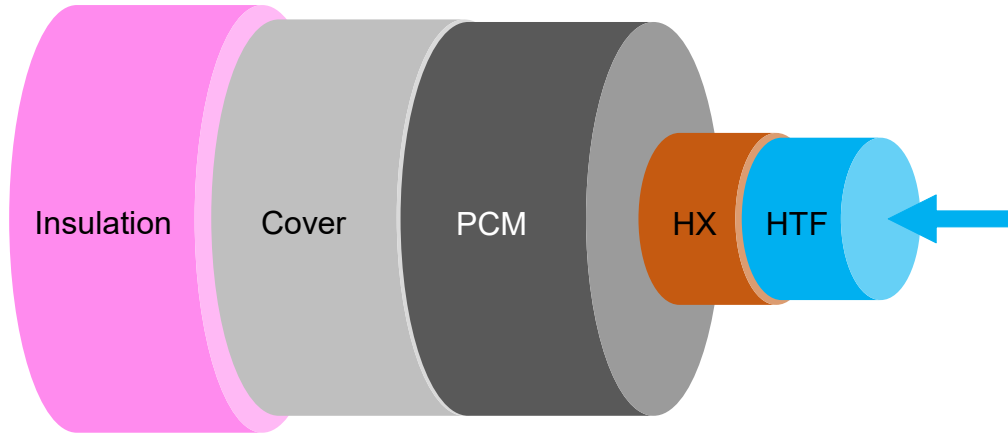


Figure S9. Illustration of a simple cylindrical geometry latent heat thermal battery.

The characteristic length L_C is simply the ratio of the PCM volume to heat exchanger surface area, giving:

$$L_C = \frac{D_o^2 - D_i^2}{4D_i} \quad (\text{S9})$$

where D_i is the inner diameter of the PCM, and D_o is the outer diameter of the PCM. Likewise, the characteristic length L_S is the ratio of PCM volume to insulated surface area:

$$L_S = \frac{D_o^2 - D_i^2}{4D_o} \quad (S10)$$

Because D_i is also the diameter of the heat exchanger pipe, it is fixed for a given heat exchanger. Then, D_o is the design parameter for the PCM geometry. As with the rectangular PCM thermal battery, there is an upper limit to L_S when the battery's total storage capacity is fixed ($L_{S,max}$), though it must be found numerically.

For the cylindrical PCM thermal battery, Eq. (S1) still applies for ΔSOC , but the expression for the thermal penetration depth (melting front location) in the cylindrical thermal battery must be found. By assuming sensible heat of the PCM liquid phase is negligible (as was assumed for the rectangular geometry thermal battery), integration of the heat equation in cylindrical coordinates for a constant heat flux at the heat exchanger/PCM interface yields the following equation for the temperature within the PCM:

$$T = T_m + \frac{Q/L}{2\pi k_L} \ln\left(\frac{D_m(t)}{D}\right) \quad (S11)$$

where $D_m(t)$ is the time varying location of the melting front. Based on the thermal conductivity and thickness of the heat exchanger pipe, the temperature of the PCM at the heat exchanger interface when the HTF temperature reaches cutoff is:

$$D_{m,cutoff} = D_i \exp\left[2k_L \left(\pi \frac{T_{cutoff} - T_m}{\dot{Q}/L} - \frac{\ln\left(\frac{D_i}{D_i - 2t_{HX}}\right)}{2k_{HX}} - \frac{1}{(D_i - 2t_{HX})h_{HTF}} \right)\right] \quad (S12)$$

where \dot{Q}/L is the rate of heat transfer per unit length of pipe, t_{HX} is the heat exchanger pipe thickness, k_{HX} is the heat exchanger material thermal conductivity, and h_{HTF} is the convection coefficient of the heat transfer fluid. It is more pertinent to find the cutoff melting front location for a fixed C-rate instead of a fixed rate of heat transfer:

$$D_{m,cutoff} = D_i \exp \left[2k_L \left(4 \frac{T_{cutoff} - T_m}{C_{rate} S_{PCM} (D_{m,cutoff}^2 - D_i^2)} - \frac{\ln \left(\frac{D_i}{D_i - 2t_{HX}} \right)}{2k_{HX}} - \frac{1}{(D_i - 2t_{HX})h_i} \right) \right] \quad (S13)$$

Plugging in the expression for L_C from Eq. (S9) into Eq. (S13) and setting the cutoff melting front location equal to the PCM outer diameter gives:

$$\sqrt{4D_i L_{C,p} + D_i^2} - D_i \exp \left[2k_L \left(\frac{T_{cutoff} - T_m}{C_{rate} S_{PCM} D_i L_{C,p}} - \frac{\ln \left(\frac{D_i}{D_i - 2t_{HX}} \right)}{2k_{HX}} - \frac{1}{(D_i - 2t_{HX})h_{HTF}} \right) \right] = 0 \quad (S14)$$

Unfortunately, Eq. (S14) cannot be solved explicitly for the cutoff thermal penetration depth, $L_{C,p}$, and it must be solved numerically. This means that the cost regime figures-of-merit cannot be found analytically. However, in Figure S10 we solve the equations numerically and find $L_{C,p}$ as a function of h_{SL} and k_L to show how these material properties affect the maximum thermal penetration depth (which will affect the device cost in the heat exchanger cost dominated regime). Figure S10 shows that $L_{C,p}$ increases with k_L and decreases with h_{SL} , though not with the same power as in the rectangular geometry of the main text. In the rectangular geometry, $L_{C,p}$ always scales with $k_L^{1/2}$ and $h_{SL}^{-1/2}$, regardless of the other material properties and operational parameters.

Meanwhile, in Figure S10a, power model regression reveals that the best fit for $L_{C,p}$ scales with $k_L^{0.30}$, and the R^2 value is 0.947. Meanwhile power model regression of Figure S10b reveals that $L_{C,p}$ scales with $h_{SL}^{-0.87}$ (with an R^2 value of 1). As such, the material properties within the PCM figures-of-merit in Fig. 5 of the main text still apply to the cylindrical geometry, though the scaling is different. It should be noted that the exponents of the thermal conductivity and latent heat (0.30 and 0.87, respectively) correspond to the PCM properties and operational parameters considered in Figure S10; if these properties and parameters change, the exponents will change as well.

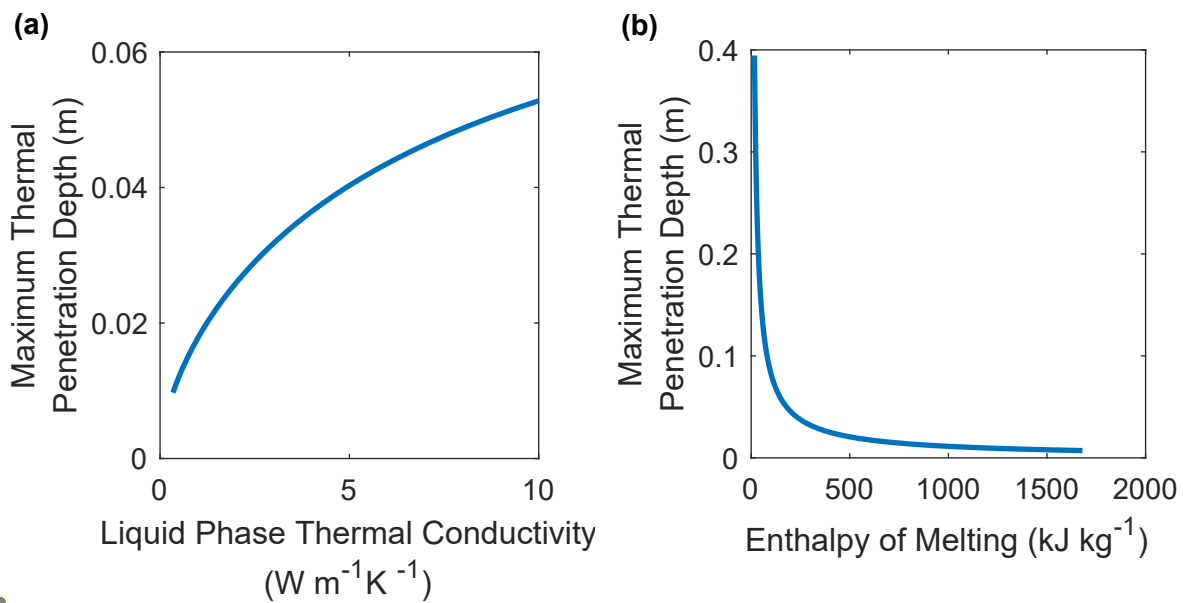


Figure S10. Maximum thermal penetration depth in a cylindrical latent heat thermal battery, as a function of liquid phase thermal conductivity (a) and enthalpy of melting (b).

Supplementary Note 12: Sensible heat thermal storage

Not only does our cost scaling analysis apply to latent heat thermal batteries, it also applies to sensible heat thermal batteries as well. In this section we consider a thermal battery with the same geometry as in Fig. 3 of the main text, but this time the thermal storage material (TSM) does

not undergo phase change. When solving for the maximum thermal penetration depth, a semi-infinite slab of TSM can be analyzed. The temperature equation for fixed heat flux into a semi-infinite slab is⁴:

$$T = T_i + \frac{q''}{k} \left(\sqrt{\frac{4\alpha t}{\pi}} \left(-\frac{x^2}{4\alpha t} \right) - x \operatorname{erfc} \left(\frac{x}{2\sqrt{\alpha t}} \right) \right) \quad (\text{S15})$$

Assuming the heat exchanger has negligible thermal mass, the temperature of the TSM at the heat exchanger interface at the instant cutoff is reached is:

$$T(x = 0, t = t_{cutoff}) = T_{cutoff} - \frac{q''}{U_{HX}} \quad (\text{S16})$$

Plugging Eq. (S15) into Eq. (S16) gives the time at which cutoff is reached:

$$t_{cutoff} = \frac{\pi k}{4\alpha} \left(\frac{T_{cutoff} - T_i}{q''} - \frac{1}{U_{HX}} \right)^2 \quad (\text{S17})$$

Yan showed that the thermal penetration depth in a rectangular slab with heat flux is $L_p = 3.21111\sqrt{\alpha t}$. The expression for the thermal penetration depth in a semi-infinite slab of TSM at the instant cutoff is reached is then:

$$L_p = 2.85k \left(\frac{T_{cutoff} - T_i}{q''} - \frac{1}{U_{HX}} \right) \quad (\text{S18})$$

However, it is more useful to derive L_p for a fixed C-rate:

$$L_p = 2.85k \left(\frac{T_{cutoff} - T_i}{S_{TSM} C_{rate} L_C \Delta SOC} - \frac{1}{U_{HX}} \right) \quad (\text{S19})$$

For the PCM, we could approximate $\Delta SOC \approx 1$ when solving for L_P with a fixed C-rate, because in that scenario all of the latent heat was being extracted (which accounted for nearly 100% of the total capacity). In the sensible heat thermal battery, there is a significant temperature drop across the TSM slab when the slab thickness is sized to be equal to the cutoff penetration depth, resulting in a ΔSOC far less than unity. Integrating Eq. (S15) to find the average temperature within the semi-infinite TSM slab between the origin and the thermal penetration depth at $t = t_{cutoff}$ gives an expression for ΔSOC :

$$(\Delta SOC)_{L_C = L_p} = \frac{0.2745 \frac{T_{cutoff} - T_i}{T_{cutoff} - T_{chg}}}{\left(1 + 0.2745 \frac{L_p S_{TSM} C_{rate}}{U_{HX}(T_{cutoff} - T_{chg})} \right)} \quad (S20)$$

Plugging Eq. (S20) into Eq. (S19), setting $L_C = L_p$, and solving the resulting quadratic equation gives the TSM thickness when it is sized to be equal to the thermal penetration depth at cutoff (for fixed C-rate):

$$L_{C,p} = \sqrt{10.37 \frac{k}{c_p \rho C_{rate}}} \quad (S21)$$

As with the latent heat thermal battery, the thickness of the TSM slab should not exceed this penetration depth. Eq. (S21) can be plugged in for L_p in Eq. (S20), yielding the ΔSOC that would result when the TSM slab is sized to the maximum thermal penetration depth.

For all TSM thicknesses less than the maximum cutoff thermal penetration depth, the semi-infinite heat transfer equation cannot be used to find ΔSOC . By assuming the temperature of the

TSM is spatially uniform at the beginning of discharge (as we did in our analysis of latent heat thermal batteries), the analytical expression for the temperature profile within a finite rectangular slab of TSM is:

$$T_{TSM} = T_i + \frac{q''}{k} \left[\left(\frac{x^2}{2L} - \frac{L}{6} \right) - \left(x - \frac{L}{2} \right) + \frac{\alpha}{L} t - \sum_{n=1}^{\infty} \frac{2L}{(n\pi)^2} \exp \left(-\alpha \left(\frac{n\pi}{L} \right)^2 t \right) \cos \left(\frac{n\pi x}{L} \right) \right] \quad (S22)$$

The equation for ΔSOC in the sensible heat thermal battery is:

$$\Delta SOC = 1 - \frac{T_{surrr} - T_{chg}}{T_{cutoff} - T_{chg}} \left(1 + \exp \left(-\frac{1}{L_S R_S'' \rho_{TSM} c_{p,TSM}} t_s \right) \right) + \frac{T_{cutoff} - \frac{1}{L_C} \int_0^{L_C} T_{TSM} dx}{T_{cutoff} - T_{chg}} \quad (S23)$$

where Eq. (S22) is used for the temperature profile within the TSM.

Using the expression for ΔSOC , the dimensionless thermal battery cost (G/G_0) was plotted as a function of L_C for the sensible heat thermal battery in Figure S11. The trends are very similar to those seen in the latent heat thermal battery, but the enthalpy of melting is replaced with the specific heat. Higher thermal conductivities allow for a larger thermal penetration depth, which drives down the device cost. Meanwhile, higher specific heat values do not significantly affect the dimensionless cost, but they do reduce the TSM cost (G_0), which in turn drives down the device cost (G).

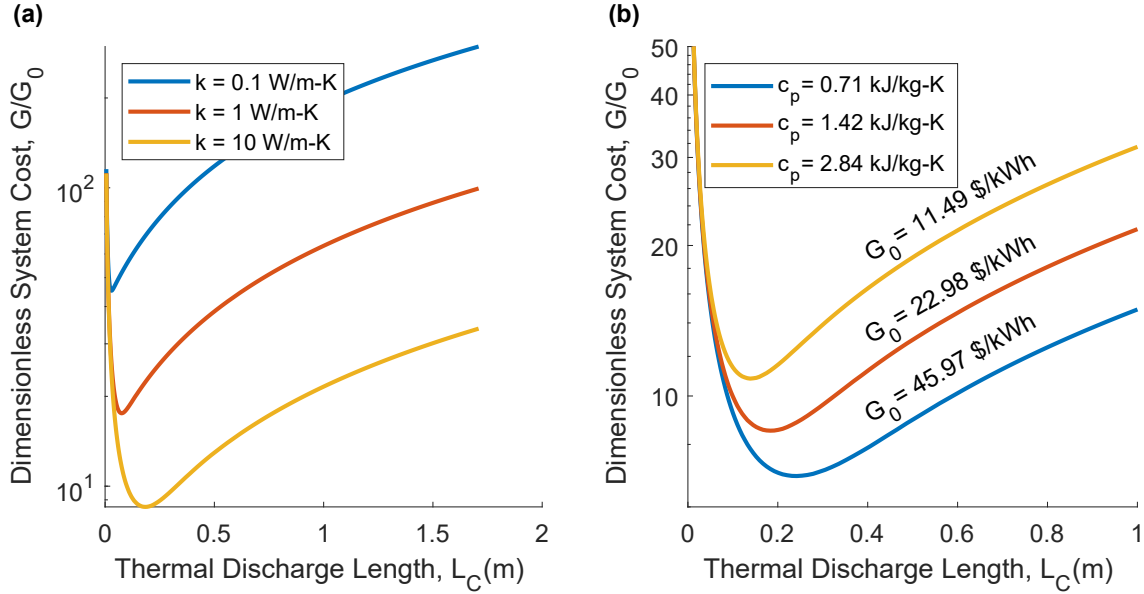


Figure S11. Dimensionless cost in a sensible heat thermal battery as a function of TSM layer thickness (which is equivalent to the thermal discharge length, L_C).

Notably, the minimum cost in Figure S11 does not occur when the TSM thickness is equal to the thermal penetration depth; instead, it occurs at smaller TSM thicknesses ($L_C < L_{C,p}$). This is because ΔSOC has a much more gradual decrease with increasing L_C in sensible heat thermal batteries than in latent heat thermal batteries. In a latent heat thermal battery, ΔSOC drops off quickly at L_C values near $L_{C,p}$, leading to $L_{C,p}$ usually being the optimal PCM thickness in latent heat thermal batteries. However, when a sensible heat storage material is used, the low ΔSOC at $L_C = L_{C,p}$ increases the TSM contribution to G significantly, leading to cost being minimized at smaller thicknesses. As the TSM material becomes cheaper, the optimal thickness moves closer to $L_{C,p}$.

As with the latent heat thermal battery, a cost regime map can be constructed for sensible heat thermal batteries, and the TSM figures-of-merit can be derived for each regime, as seen in

Figure S12. The figures-of-merit are nearly identical to the latent heat thermal battery figures-of-merit, except that the enthalpy of melting has been replaced with the specific heat of the TSM. These FOMs were derived from Eq. (S15) – (S23).

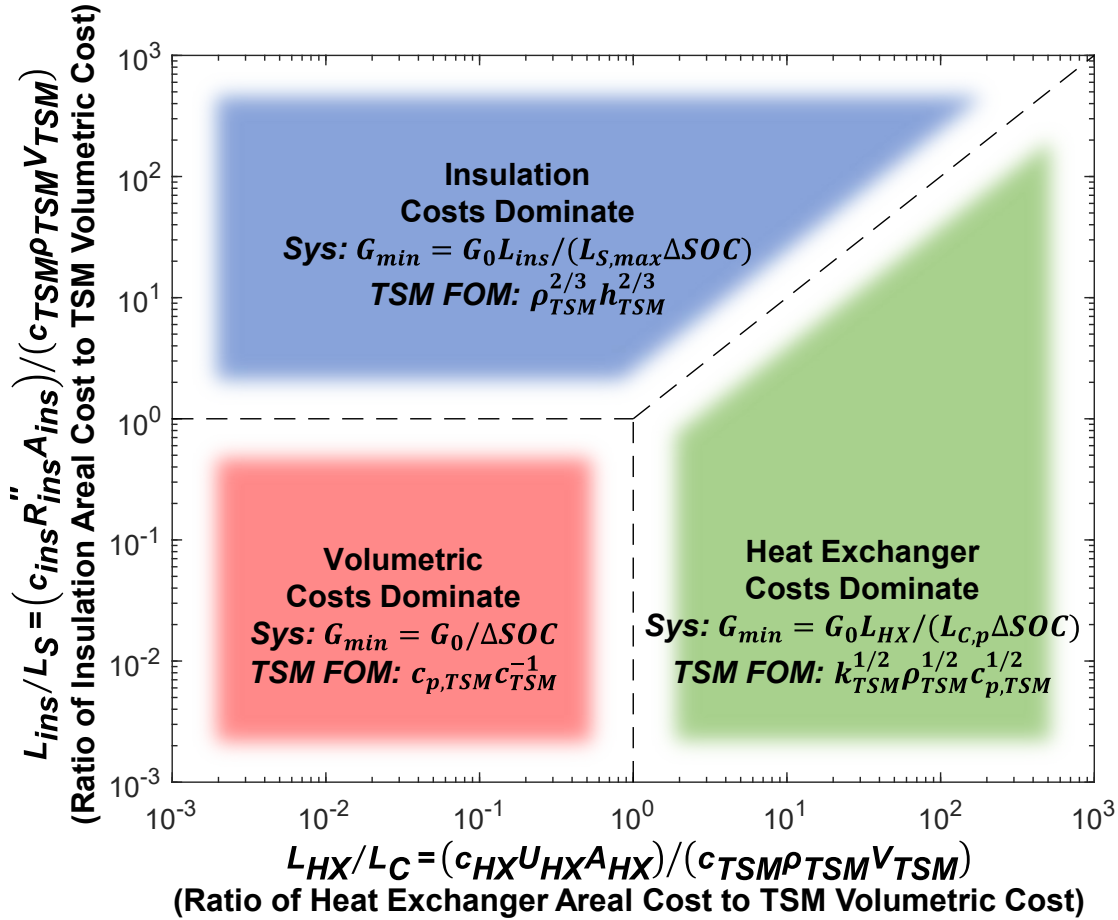


Figure S12. Cost regime map for a sensible heat thermal battery. Just as with the latent heat thermal battery in the main text of this work, there are three regimes where different costs dominate, and each regime has a thermal storage material figure-of-merit.

Eq. (S8) for $L_{S,max}$ still applies to the rectangular sensible heat thermal battery, since it is geometry dependent (not material dependent).

Supplementary Note 13: Table of cost inputs

Below is a table of the cost inputs used to generate the different figures within this work, including figures in both the main text and SI.

Table S1. Values used in cost analyses.

Variable	Symbol	Value
Liquid phase PCM thermal conductivity [$\text{W m}^{-1} \text{K}^{-1}$]	k_L	Varied (Fig. 2a, Figure S8, Figure S10a)
		10 (Fig. 2b-d, Fig. 3 “n-Tetradecane + Graphite” “BTO Target Material”, Fig. 4, Fig. 5 “n-Tetradecane + Graphite” “Ice + Graphite” “BTO Target (Low Thermal Conductivity) + Graphite”, Fig. 6 “n-Tetradecane + Graphite”, Figure S2, Figure S3, Figure S4 “n-Tetradecane + Graphite”, Figure S5 “n-Tetradecane + Graphite”, Figure S6, Figure S10b)
		0.2 (Fig. 3 “n-Tetradecane”, Fig. 5 “n-Tetradecane”, Fig. 6 “n-Tetradecane”, Figure S4 “n-Tetradecane”, Figure S5 “n-Tetradecane”)
		0.6 (Fig. 2e, Fig. 3 “Ice”, Fig. 5 “Ice”)
		100 (Figure S5d)
Sensible storage material thermal conductivity [$\text{W m}^{-1} \text{K}^{-1}$]	k_{TSM}	1 (Fig. 5 “BTO Target (Low Thermal Conductivity)”, Figure S7)
		Varied (Figure S11a)
Latent heat of melting [kJ kg^{-1}]	h_{SL}	10 (Figure S11b)
		167.98 (Fig. 3 “n-Tetradecane”, Fig. 5 “n-Tetradecane”, Fig. 6 “n-Tetradecane”, Figure S2, Figure S3, Figure S4 “n-Tetradecane”, Figure S5 “n-Tetradecane”, Figure S6, Figure S10a)
		334 (Fig. 2e, Fig. 3 “Ice”, Fig. 5 “Ice”)
		180 (Fig. 3 “BTO Target Material”, Fig. 5 “BTO Target Material”)

		134.38 (Fig. 2a,c-d, Fig. 3 “n-Tetradecane + Graphite”, Fig. 4, Fig. 5 “n-Tetradecane + Graphite”, Fig. 6 “n-Tetradecane + Graphite”, Figure S4 “n-Tetradecane + Graphite”, Figure S5 “n-Tetradecane + Graphite”)
		267.2 (Fig. 5 “Ice + Graphite”)
		144 (Fig. 5 “BTO Target Material + Graphite”)
		Varied (Fig. 2b, Figure S7, Figure S8, Figure S10b)
		1679.8 (Figure S5a)
Heat exchanger thermal conductance [$\text{W m}^{-2} \text{K}^{-1}$]	U_{HX}	570 (Fig. 2, Fig. 4, Fig. 5, Fig. 6, Figure S2, Figure S3, Figure S4, Figure S5, Figure S6, Figure S11)
Insulation thermal resistance [$\text{m}^2 \text{K W}^{-1}$]	R_{ins}''	16480 (Figure S7, Figure S8) 5.28 (Fig. 2, Fig. 4, Fig. 5, Figure S3, Figure S4, Figure S5, Figure S6, Figure S11)
Storage time [h]	t_s	$\rightarrow \infty$ (Fig. 6, Figure S7, Figure S8) 12 (Fig. 2, Fig. 4, Fig. 5 “C/4” “1C”, Figure S3, Figure S4, Figure S5, Figure S6, Figure S7, Figure S8, Figure S11)
Cost of PCM [$\$ \text{kg}^{-1}$]	c_{PCM}	24 (Fig. 5 “C/24”) 2 (Fig. 2a-b,d, Fig. 3 “n-Tetradecane” “n-Tetradecane + Graphite”, Fig. 4, Fig. 5 “n-Tetradecane” “n-Tetradecane + Graphite”, Fig. 6, Figure S3, Figure S5, Figure S6, Figure S8)
		0.015 (Fig. 2e, Fig. 3 “Ice”, Fig. 5 “Ice”)
		0.75 (Fig. 3 “BTO Target Material”, Fig. 5 “BTO Target Material”)
		0.41 (Fig. 5 “Ice + Graphite”)
		1 (Fig. 5 “BTO Target Material + Graphite”)
		1.8 (Figure S4)
		Varied (Fig. 2c)

		20 (Figure S7)
Cost of sensible storage material [\$ kg ⁻¹]	c_{TSM}	0.2 (Figure S11)
PCM density [kg m ⁻³]	ρ_{PCM}	836 (Fig. 3 “n-Tetradecane”, Fig. 5 “n-Tetradecane”, Fig. 6 “n-Tetradecane”, Figure S2, Figure S3, Figure S4 “n-Tetradecane”, Figure S5 “n-Tetradecane”, Figure S6, Figure S7, Figure S8, Figure S10)
		1000 (Fig. 2e, Fig. 5 “Ice”)
		2000 (Fig. 5 “BTO Target Material”)
		1121 (Fig. 2a-d, Fig. 3 “n-Tetradecane + Graphite”, Fig. 4, Fig. 5 “n-Tetradecane + Graphite”, Fig. 6 “n-Tetradecane + Graphite”, Figure S4 “n-Tetradecane + Graphite”, Figure S5 “n-Tetradecane + Graphite”)
		1252 (Fig. 5 “Ice + Graphite”)
		2052 (Fig. 5 “BTO Target Material + Graphite”)
Sensible storage material density [kg m ⁻³]	ρ_{TSM}	836 (Figure S11)
Solid phase PCM specific heat [kJ kg ⁻¹ K ⁻¹]	$c_{p,s}$	1.42 (Fig. 3 “n-Tetradecane”, Fig. 5 “n-Tetradecane”, Fig. 6 “n-Tetradecane”, Figure S2, Figure S3, Figure S4 “n-Tetradecane”, Figure S5 “n-Tetradecane”, Figure S6, Figure S7, Figure S8, Figure S10)
		1.28 (Fig. 2a-d, Fig. 3 “n-Tetradecane + Graphite”, Fig. 4, Fig. 5 “n-Tetradecane + Graphite”, Fig. 6 “n-Tetradecane + Graphite”, Figure S4 “n-Tetradecane + Graphite”, Figure S5 “n-Tetradecane + Graphite”)
		2.09 (Fig. 2e, Fig. 3 “Ice” “BTO Target Material”, Fig. 5 “Ice” “BTO Target Material”)
Sensible storage material specific heat [kJ kg ⁻¹ K ⁻¹]	$c_{p,TSM}$	1.42 (Figure S11)
C-rate [h ⁻¹]	C_{rate}	1 (Fig. 2a-c, Fig. 3b, Fig. 4, Figure S2, Figure S3, Figure S4, Figure S5(a,c,d), Figure S6, Figure S7, Figure S8, Figure S10, Figure S11)

		¼ (Fig. 3a)
		Varied (Fig. 2d-e, Fig. 5, Fig. 6, Figure S4, Figure S5)
		0.1 (Figure S5b)
Thermal battery capacity [kWh]	Cap	21.1 (Fig. 4)
Cutoff temperature [°C]	T_{cutoff}	12 (Fig. 2, Fig. 3, Fig. 4, Fig. 5, Fig. 6, Figure S2, Figure S3, Figure S4, Figure S5, Figure S6, Figure S7, Figure S8, Figure S10, Figure S11)
Charge temperature [°C]	T_{chg}	-10 (Fig. 2, Fig. 3, Fig. 4, Fig. 5, Fig. 6, Figure S3, Figure S4, Figure S5, Figure S6, Figure S7)
		4 (Figure S2)
		4.6 (Figure S8)
Surrounding ambient temperature [°C]	T_{surr}	20 (Fig. 2, Fig. 3, Fig. 4, Fig. 5, Figure S3, Figure S4, Figure S5, Figure S6, Figure S7, Figure S8, Figure S11)
PCM melting temperature [°C]	T_m	4.6 (Fig. 2a-d, Fig. 3 “n-Tetradecane” “n-Tetradecane + Graphite”, Fig. 4, Fig. 5 “n-Tetradecane” “n-Tetradecane + Graphite”, Fig. 6, Figure S2, Figure S3, Figure S4, Figure S5, Figure S6, Figure S7, Figure S8, Figure S10)
		0 (Fig. 2e, Fig. 3 “Ice”, Fig. 5 “Ice” “Ice + Graphite”)
		5 (Fig. 3 “BTO Target Material”, Fig. 5 “BTO Target Material” “BTO Target Material + Graphite”)
Heat exchanger cost [\$ K W ⁻¹]	c_{HX}	0.18 (Figure S3, Figure S5(a-b), Figure S11)
		0.09 (Fig. 2, Fig. 3, Fig. 4, Fig. 5, Fig. 6a-b, Figure S4)
		0.018 (Fig. 6c-d)
		0.009 (Figure S5(c-d))
		1.8 (Figure S4c)
		0.02 (Figure S4d, Figure S6)
		6.4×10^{-3} (Figure S7)

		2.6×10^{-3} (Figure S8)
Insulation cost [$\$ \text{W m}^{-4} \text{K}^{-1}$]	c_{ins}	23.1 (Fig. 2, Fig. 3, Fig. 4, Fig. 5, Figure S3, Figure S6, Figure S11)
		231 (Figure S4e)
		2.3 (Figure S4f)
		0 (Fig. 6, Figure S7, Figure S8)
Heat exchanger thickness [m]	t_{HX}	1×10^{-3} (Fig. 2, Fig. 3, Fig. 4, Fig. 5, Fig. 6, Figure S4, Figure S5)
Heat exchanger thermal conductivity [$\text{W m}^{-1} \text{K}^{-1}$]	k_{HX}	200 (Figure S10)
Heat transfer fluid convection coefficient [$\text{W m}^{-2} \text{K}^{-1}$]	h_{HTF}	500 (Figure S10)
Characteristic thermal discharge length [m]	L_C	Varied (Fig. 2, Fig. 3, Fig. 4, Figure S2, Figure S3, Figure S4, Figure S5, Figure S6, Figure S11)
		$L_{C,p}$ (Fig. 5, Fig. 6, Figure S4, Figure S5, Figure S7, Figure S8)
Characteristic thermal storage length [m]	L_S	0.01 (Fig. 2, Fig. 3, Figure S3, Figure S6)
		Varied (Fig. 4, Figure S4, Figure S5)
		$L_{S,max}$ (Fig. 5, Figure S7, Figure S8)
		0.52 (Figure S11)

Supplementary Note 14: State of charge

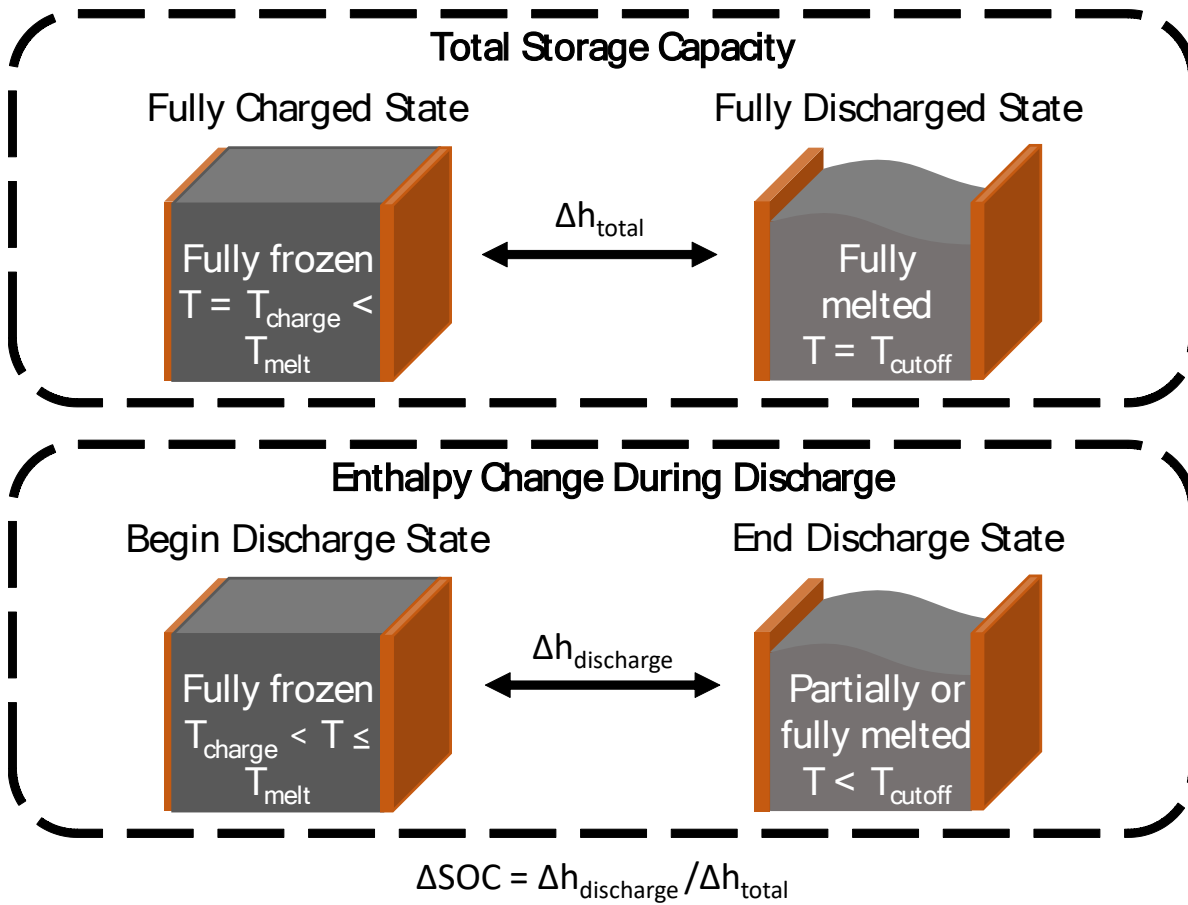


Figure S13. The quantity ΔSOC is defined as the ratio of the enthalpy change during discharge to the enthalpy change between the fully charged and fully discharged states. The fully charged state is defined as the fully frozen PCM at some charged temperature that is below the melting point (*i.e.*, the solid is subcooled). However, when discharging begins, the PCM is at some temperature higher than the initial charged state temperature, due to heat leaking into the thermal battery during storage, though it is still entirely frozen. The fully discharged state is defined as the PCM fully melted and uniformly at the cutoff temperature. However, during the actual discharge, the heat exchanger temperature reaches the cutoff value before the PCM does, meaning the PCM is at some temperature lower than the cutoff temperature at the end of discharge state. In fact, depending on the PCM dimensions, some of the PCM may still be frozen at the end of discharge.

References

1. Woods, J. *et al.* Rate capability and Ragone plots for phase change thermal energy storage. *Nat. Energy* **6**, 295–302 (2021).
2. Jiji, L. M. *Heat conduction*. (Springer, 2009).
3. Owens Corning R-30 Unfaced Fiberglass Insulation Batt 16 in. x 48 in. (8-Bags) C84A. *The Home Depot* <https://www.homedepot.com/p/Owens-Corning-R-30-Unfaced-Fiberglass-Insulation-Batt-16-in-x-48-in-8-Bags-C84A/301274917>.
4. Çengel, Y. A. & Ghajar, A. J. *Heat and mass transfer: fundamentals & applications*. (McGraw Hill Education, 2015).